IEEE Access
Multidisciplinary | Rapid Review | Open Access Journal

Received June 22, 2020, accepted July 13, 2020, date of publication July 17, 2020, date of current version July 28, 2020.

Digital Object Identifier 10.1109/ACCESS.2020.3010007

Unified Boundary Control With Phase Shift Compensation for Dual Bridge Series Resonant DC-DC Converter

GUO CHEN, XIAODONG LI, (Senior Member, IEEE), AND SHENGZHI ZHOU
Faculty of Information Technology, Macau University of Science and Technology, Taipa, Macau

Corresponding author: Xiaodong Li (xdli@must.edu.mo)

This work was supported in part by the Fundo para o Desenvolvimento das Ciencias e da Tecnologia of Macau under Grant 0065/2019/A2.

ABSTRACT In this paper, the triple-phase-shift (TPS) control with certain unified boundary conditions is applied to a dual-bridge series resonant converter (DBSRC) for applications needing bidirectional energy flow ability. The control strategy is unified for the whole variation range of load, input/output voltage and with simple calculation. By using this unified boundary control, the circulating energy is minimized significantly. A wide soft switching operation range can be achieved as well. Furthermore, based on the analysis results of unified boundary conditions, an improved unified boundary control with duty cycle compensation is also proposed. The ZVS operations of all sides switches can be maintained for wide converter gain and load with high efficiency. The procedure of design for important parameters is given. Finally all works are verified through actual experimental tests on a 500W laboratory prototypes successfully.

INDEX TERMS DC-DC conversion, resonant converter, phase-shift modulation, soft switching.

I. INTRODUCTION

Due to the problems of global warming and energy crisis, the technology and application of renewable energy have been widely studied [1], [2]. A high frequency (HF) isolated bidirectional DC-DC converter (IBDC) is a key power interface for renewable energy systems. Dual-active-bridge (DAB) DC-DC converter was initially proposed in [3], which is typical type of IBDC. A DAB converter consists of two active full bridges linked through a HF transformer and a series inductor. DAB converters have shown many competitive advantages such as high power density, high reliability, high efficiency, symmetrical circuit structure, simple control strategies, and so on [4]–[7]. Since a DAB converter is operated with high switching frequency, the size of reactive component and lower frequency related noise will be reduced [8]–[12]. The double-bridge series resonant converter (DBSRC) is a resonant version of DAB and also a powerful choice for achieving high power density. With the high frequency, the size of reactive component of DBSRC will be small too. Due to the resonance characteristics, there are some extra features in DBSRC [13]–[17]. Compared with DAB, the current in DBRC is almost sinusoidal due to the lower pass feature of resonant tank, which will lead to smaller higher order harmonics and reduce the size of filter. The fundamental harmonics approximation (FHA) approach can be employed to simply the mathematical models of DBSRC. Besides these, the resonant capacitor can also server as DC-blocking capacitor, which can prevent the transformer from saturation. In this paper, the research would be performed on a HF DBSRC.

Until now, there are four types of control schemes mainly used for DAB and DBSRC converters [18]–[22]. The most commonly used scheme is single-phase-shift (SPS) control because it has the advantages of simple controller and easy implementation with one controllable phase-shift angel. However, with the variation of voltage gain and load level, the circulation energy becomes much higher, and its efficiency is greatly lowered. Extended-phase-shift (EPS) control is an improved version with one more controllable phase-shift angel. Compared with SPS control, EPS control can reduce circulating energy and expand soft-switching range. However, when the power flow direction is changed, the working modes of the two bridges need to be exchanged to reduce circulating energy. Dual-phase-shift (DPS) control is easier to implement than EPS control, because the inner phase-shift angles in two bridges are equal. With DPS control,

The associate editor coordinating the review of this manuscript and approving it for publication was Zhehan Yi.

the converter dynamic performance may be improved. However, the improvement of efficiency is not significantly in some operating regions. Triple-phase-shift (TPS) is a unified form of phase-shift control, while SPS, DPS and EPS can also be regarded as special cases of TPS control. The TPS control is the most complex but flexible control scheme, so that it was reported in many research works for optimization modulation with performance improvement in the DAB converter [20], [23].

A universal TPS model based on fundamental-optimal strategy was reported in [24]. The circuit design and optimization is based on fundamental harmonics approximation (FHA) analysis, which can reduce calculation complexity. And low circulating current is obtained. When input voltage matched output voltage, the strategy can ensure the soft-switching working. However, ZVS performance will degrade under non-unity voltage gain. The boundary Trapezoidal Modulation (TZM) control based on TPS scheme with fixed duty cycle and magnetizing current compensation was proposed in [25]. This strategy is simple and can be implemented with better performance. However, ZVS performance will degrade under light load conditions. And the additional conduction loss is introduced by compensated magnetizing current, which will degrade converter efficiency under light load. Based on particle-swarm algorithm, a optimal TPS modulation strategy was proposed in [26] to minimize the reactive power. But whole-range ZVS operation of the DAB converter is not ensure when variation of voltage gain is wide. Since the calculation is complex, the implementation of control is difficult and costly in practice.

In [27] and [28], minimum current trajectory (MCT) and modified minimum current trajectory (M-MCT) were proposed, which achieve minimum-tank-current operation. Three phase-shift angles are defined and only two phase-shift angles are adopted, which is according to the range of voltage gain. Thus, the selection of control variable is not unified and usually relied on a lookup table stored in DSP controller. And when operated under the light load conditions, both of MCT and M-MCT suffer from the hard switching. Meanwhile, when the load level is high or the converter gain is away from unity, high circulation current will occur in the input bridge especially. So, converter efficiency will be degraded under variation of voltage gain and load level.

A complex modulation strategy with four degrees of freedom was reported in [29]. Switching frequency is adopted as additional modulation variable. This strategy achieve wide range ZVS operation range with no circulation power. Since four controllable variables are adopted in the converter modulation, it makes the optimization of circuit parameters quite complicated. Furthermore the selections of control variables are not unified, than increase the computational burden of the controller.

Taking into account of flexibility, effectiveness and complexity of four control schemes, in this paper, the TPS control scheme is adopted. To address the problem of complex calculation, operation mode transition and narrow softer switching region, the TPS control with certain unified boundary condition will be applied to a DBSRC. The control strategy is flexible, unified and with simple calculation. By using this unified boundary control, the circulating energy is minimized significantly. A wide soft switching operation range can be achieved as well.

The steady-state analysis of the DBSRC is performed using fundamental harmonics approximation (FHA) approach at first. Then the operation principle for unified boundary control is then discussed. Furthermore, based on the analysis results, an improved unified boundary control with duty cycle compensation is proposed. It can be seen that ZVS operations of all sides switches are maintained for wide converter gain and load. As an example, the application of unified boundary control has been examined in a DBSRC, which is able to suppress circulating energy and maintain soft switching operation for all switches at variation of converter gain and load. Finally, all works are verified through actual experimental tests on a laboratory prototype converter.

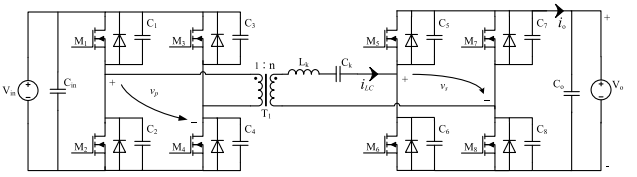

FIGURE 1. Basic topology of a dual-bridge series resonant converter.

II. STEADY-STATE ANALYSIS OF DBSRC WITH TPS CONTROL

A. PRINCIPLE OF DSBRC WITH TPS CONTROL

Fig. 1 shows the circuit configuration of a DBSRC. Both the primary side and the secondary are active full-bridges. The two symmetric full-bridges are connected by a series LC-type resonant tank and a HF transformer T_1. The two voltage sources V_{in} and V_o are the primary side voltage and the secondary side voltage, respectively. The primary side bridge is implemented by four switches $M_1 - M_4$, and the secondary side bridge is constructed by four switches $M_5 - M_8$. $C_1 - C_8$ are the output parasitic capacitors of switches $M_1 - M_8$, respectively. C_{in} and C_o are filter capacitors on the input side and output side, respectively. The leakage inductance of the HF transformer is utilized as part of resonant inductance L_k. The series capacitor C_k used in the resonant tank will help in preventing the transformer from saturation. With the assumption of an infinite magnetizing inductance of the transformer, the capacitor can split and be implemented on both side of the transformer. Hence, saturation on the primary-side full-bridge can also be prevented. HF transformer T_1 with a turns ratio of $1 : n$ provides functions of electrical isolation and voltage level conversion.

The operation principle of conventional TPS control is shown in Fig. 2. Energy is exchanged bidirectionally between the primary side voltage source V_{in} and the secondary voltage source V_o due to the symmetric structure of DBSRC.

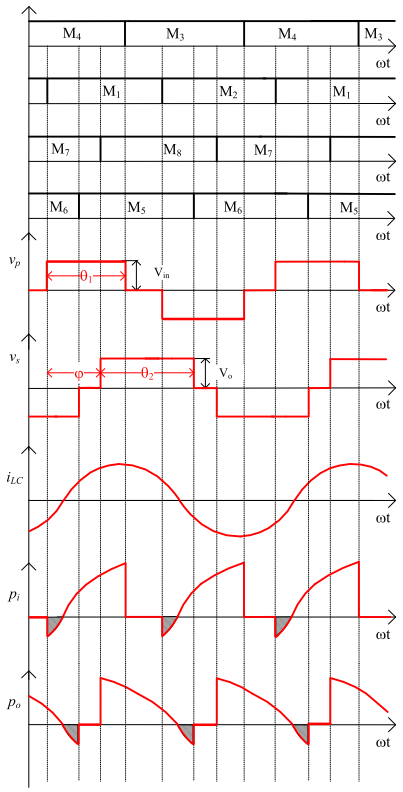

FIGURE 2. Typical operating waveforms of the DBSRC under conventional TPS control with all switches working in ZVS.

The power transfer from the primary side to the secondary side is defined as a forward power flow. It is seen that all switches are operating alternatively at almost 50% duty cycle with necessary dead-time. Three phase-shift angles are defined here for bidirectional power regulation. The inner-bridge phase-shift θ_1 is defined as the phase-shift by which the driver signal of M_1 leads that of M_3 in the primary side bridge. θ_1 is in the range of $[0,\pi]$. The inner-bridge phase-shift θ_2 is defined as the phase-shift by which the driver signal of M_6 lags that of M_8 in the secondary side bridge. The range of θ_2 is $[0,\pi]$. Thus, the obtained two high frequency ac voltages v_p and v_s are no longer traditional square-wave voltage due to the existence of internal phase-shift. The external phase-shift φ is defined as the phase-shift by which the driver signal of M_1 leads that of M_8. The external phase-shift φ can also be defined as the phase-shift by which the positive rising edge of v_p from zero to high level leads that of v_s during one switching period. The range of φ depends on the direction of power and the values of θ_1 and θ_2. Both the instantaneous input power p_i and output power p_i are discontinuous, and can be controlled by the combination of three phase-shift angles.

B. FHA ANALYSIS FOR DBSRC WITH TPS CONTROL

When the switching frequency is close to the resonant frequency, FHA analysis is adopted for the steady state analysis with simplified calculation and acceptable accuracy. The obtained equations can be used for a quick initial converter design with enough accuracy. All parameters have been reflected to the secondary side (denoted by a superscript "′", if the parameter is on the primary side). In order to obtain normalized equations, the following base values are chosen:

$$V_B = nV_{in};\ Z_B = \frac{V_o^2}{P_R};\ I_B = \frac{V_B}{Z_B};$$
$$f_B = f_r = \frac{1}{2\pi\sqrt{L_k C_k}};\ P_B = \frac{V_B^2}{Z_B} \tag{1}$$

where f_r is the series resonance frequency, P_R is the rated output power.

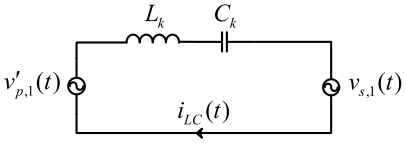

FIGURE 3. Equivalent circuit for fundamental components in time domain.

In Fig. 3, the fundamental equivalent circuit of DBSRC is given. The normalized two voltage sources of v'_p and v_s in time domain with only fundamental components can be expressed as:

$$v'_{p,1pu}(\omega_s t) = \frac{4}{\pi}\sin\frac{\theta_1}{2}\sin(\omega_s t) \tag{2}$$
$$v_{s,1pu}(\omega_s t) = \frac{4M}{\pi}\sin\frac{\theta_2}{2}\sin\left[\omega_s t - (\varphi + \frac{\theta_2-\theta_1}{2})\right] \tag{3}$$

where the converter gain M is defined as $M = \frac{V_o}{nV_{in}}$, ω_s is the switching angular frequency. It is seen from (3) that the fundamental component of v'_p leads that of v_s with a phase-shift angle of $\varphi + \frac{\theta_2-\theta_1}{2}$.

The normalized impedance of the resonant tank can be written as:

$$X_{s,pu} = (\omega_s L_k - \frac{1}{\omega_s C_k})/Z_B = Q(F - 1/F) \tag{4}$$

where rated load quality factor Q is defined as $Q = \frac{\omega_r L_k}{Z_B} = \frac{1}{\omega_r C_k Z_B}$, the normalized switching frequency F can be expressed as $F = \frac{\omega_s}{\omega_r}$, and ω_r is the resonant angular frequency.

Then the normalized resonant tank current $i_{LC,pu}$ in time domain with only fundamental component can be found as:

$$i_{LC,pu}(\omega_s t) = \frac{4\left[M\sin\frac{\theta_2}{2}\cos(\omega_s t-(\varphi+\frac{\theta_2-\theta_1}{2}))-\sin\frac{\theta_1}{2}\cos(\omega_s t)\right]}{\pi X_{s,pu}} \tag{5}$$

By using (5), the normalized root-mean-square (rms) current $I_{LCr,pu}$ is given as:

$$I_{LCr,pu} = \frac{\sqrt{8}\sqrt{M^2\sin^2\frac{\theta_2}{2}-2M\sin\frac{\theta_1}{2}\sin\frac{\theta_2}{2}\cos(\varphi+\frac{\theta_2-\theta_1}{2})+\sin^2\frac{\theta_1}{2}}}{\pi X_{s,pu}} \tag{6}$$

The normalized resonant tank capacitor peak voltage can be evaluated as follows:

$$V_{Cp,pu} = \frac{4\sqrt{M^2\sin^2\frac{\theta_2}{2} - 2M\sin\frac{\theta_1}{2}\sin\frac{\theta_2}{2}\cos(\varphi+\frac{\theta_2-\theta_1}{2}) + \sin^2\frac{\theta_1}{2}}}{\pi\left(F^2-1\right)} \tag{7}$$

Ignoring the circuit loss, the normalized average transferred power with TPS control in a switching cycle can be evaluated from either side of the converter, which can be calculated as:

$$\begin{aligned} P_{o,pu} &= \frac{1}{2\pi}\int_0^{2\pi} v'_{p,1pu}(\omega_s t) i_{LC,pu}(\omega_s t) d\omega_s t \\ &= \frac{8M}{\pi^2 X_{s,pu}} \sin\frac{\theta_1}{2}\sin\frac{\theta_2}{2}\sin(\varphi+\frac{\theta_2-\theta_1}{2}) \end{aligned} \tag{8}$$

By using (1), the normalized power can also be defined as:

$$P_{o,pu} = \frac{P_o}{P_B} = \frac{P_o}{P_R}\frac{{V_o}^2}{(nV_{in})^2} = M^2 G \tag{9}$$

where P_o is the actual output power, and $G \in [0, 1]$ is the percentage of the power level index at certain voltage gain, which is defined as:

$$G = \frac{P_o}{P_R} = \frac{P_{o,pu}}{M^2} \tag{10}$$

Substituting (8) into (10), the voltage gain can also be defined as:

$$M = \frac{8}{\pi^2 G X_{s,pu}} \sin\frac{\theta_1}{2}\sin\frac{\theta_2}{2}\sin(\varphi+\frac{\theta_2-\theta_1}{2}) \tag{11}$$

Equation (11) shows the relationship between the power level index and the voltage gain in a DBSRC under TPS modulation. The control phase-shift θ_1, θ_2 and φ shall be adjusted dynamically with the changes of G and M to keep the balance in (11).

III. THE PROPOSED UNIFIED BOUNDARY CONTROL

A. PROPOSED UNIFIED BOUNDARY CONTROL

It can be seen from Fig. 2 that DBSRC operating under conventional TPS control with all switches in ZVS does not guarantee complete elimination of circulating energy (marked by shadow part of instantaneous input power p_i and output power p_o). The high backflow power would cause high rms resonant tank current and hence lead to high switches conduction loss. So in this work, the optimization object for selecting a control scheme is to depress circulating energy and, meanwhile, to achieve a wide soft switching operation range.

A unified boundary control based on TPS control is proposed to eliminate circulating energy and extend soft switching operation range. The working principle of unified boundary control is depicted in Fig. 4. In order to simplify calculating, the effect of dead band is neglected. Since unified boundary TPS control is a special case of TPS control,

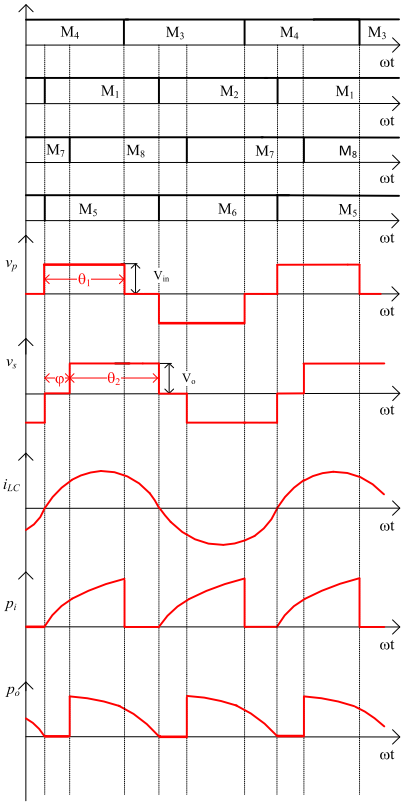

FIGURE 4. Typical operating waveforms of the DBSRC under unified boundary TPS control.

the definitions of three phase shift angles are the same as conventional TPS control. The obtained equations (1)-(8) are suitable for unified boundary TPS control with certain boundary conditions. The constraints can be derived as follows.

To completely eliminate secondary side circulating energy, the falling edge of v_s (turn-on moments of M_5 and M_6) should move left and finally align with the zero crossing point of resonant tank current i_{LC} as shown in Fig. 4. Since the resonant tank current i_{LC} is a sinusoidal waveform, the first boundary condition of the two angles can be easily written as

$$\pi = \varphi + \theta_2 \tag{12}$$

To completely eliminate primary side circulating energy, the rising edge of v_p (turn-on moments of M_1 and M_2) should move right and eventually align with the zero crossing point of resonant tank current i_{LC} as shown in Fig. 4. By using (5), the zero circulating energy condition can be expressed as

$$i_{LC,pu}(\frac{\pi-\theta_1}{2}) = \frac{4\left[-\sin^2\frac{\theta_1}{2} + M\sin\frac{\theta_2}{2}\sin(\varphi+\frac{\theta_2}{2})\right]}{\pi X_{s,pu}} = 0 \tag{13}$$

With the help of (12), the secondary boundary condition (13) can be simplified as

$$\sin\frac{\theta_1}{2} = \sqrt{M}\sin\frac{\theta_2}{2} \tag{14}$$

Based on the above analysis, the output power can be controlled solely by the external phase-shift φ under the unified boundary TPS control. The other two phase-shift angles (θ_1 and θ_2) can be represented by φ from (12) and (14). Substituting (12) and (14) into (8), the normalized output power under unified boundary TPS control can be rewritten as

$$P_{o,pu} = \frac{8M^{\frac{3}{2}}}{\pi^2 X_{s,pu}} \cos^2\frac{\varphi}{2} \cos\left[\arcsin(\sqrt{M}\cos\frac{\varphi}{2}) - \frac{\varphi}{2}\right] \quad (15)$$

The normalized output power $P_{o,pu}$ with respect to φ for different values of gain M under the unified boundary TPS control is plotted in Fig. 5. It can be seen that for a fixed voltage gain, the power curve is a convex function of φ, which has a global maximum. The peak normalized output power $P_{o,pu}$ is proportional to the voltage gain M. Meanwhile, a small range of φ can regulate the net power from partial load to full load.

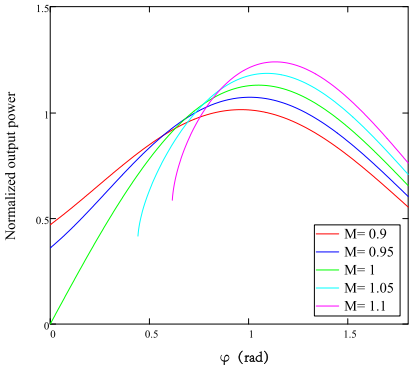

FIGURE 5. Normalized output power $P_{o,pu}$ versus external phase-shift angle φ ($Q = 1$, $F = 1.26$).

B. STEADY STATE ANALYSIS IN PHASOR DOMAIN

To make the control strategy understandable, the phasor diagrams to illustrate power regulations for positive power are presented in Fig. 6. Generally to achieve a lower load for any converter gain, the magnitudes of two voltage vectors ($\mathbf{V_{s,1}}$ and $\mathbf{V'_{p,1}}$) will be increased, and the angel between them will be reduced to keep the balance in (8). Meanwhile, the magnitude of resonant tank current phasor $\mathbf{I_{LC}}$ will decrease. As illustrated in Fig. 6(a), for the case of $M = 1$, the magnitudes of two ac voltage vector $\mathbf{V_{s,1}}$ and $\mathbf{V'_{p,1}}$ are isometric. The soft switching operation can be realized at whole load operation. As plotted in Fig. 6(b), for the case of $M < 1$, the magnitude of ac voltage vector $\mathbf{V_{s,1}}$ is shorter than that of $\mathbf{V'_{p,1}}$. As shown in Fig. 6(c), for the case of $M > 1$, the magnitude of ac voltage vector $\mathbf{V_{s,1}}$ is longer than that of $\mathbf{V'_{p,1}}$. Therefore, the limit to keep the unified boundary TPS control defined in (12) and (14) can be obtained as:

$$\begin{cases} \theta_2 = \pi & \text{if} \quad M \le 1 \\ \theta_1 = \pi & \text{if} \quad M > 1 \end{cases} \quad (16)$$

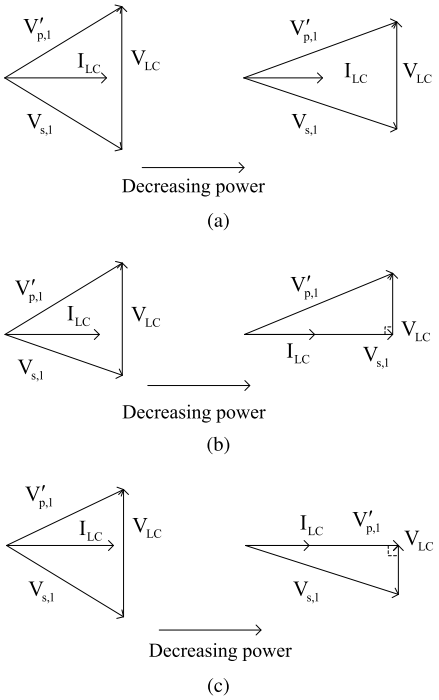

FIGURE 6. Phasor diagrams of the unified boundary control strategy for positive power transfer. (a) $M = 1$. (b) $M < 1$. (c) $M > 1$.

With the boundary condition (16), it can be seen from the phasor diagrams that the tank current phasor $\mathbf{I_{LC}}$ is in phase with secondary side voltage vectors ($\mathbf{V_{s,1}}$) when $M \le 1$ and in phase with primary side voltage vectors ($\mathbf{V'_{p,1}}$) when $M > 1$. By substituting (16) into (12) and (14), the boundary normalized power of losing full softer switching for unified boundary control can be expressed as:

$$P_{oB,pu} = \begin{cases} \dfrac{8M\sqrt{M - M^2}}{\pi^2 X_{s,pu}} & \text{if } M \le 1 \\ \dfrac{8M\sqrt{1/M - 1/M^2}}{\pi^2 X_{s,pu}} & \text{if } M > 1 \end{cases} \quad (17)$$

C. EVALUATION OF SOFT SWITCHING PERFORMANCE

To realize zero-voltage switching (ZVS), the necessary condition is to have a non-zero instantaneous resonant tank currents at the turn-on instances to charge/discharge the switches parasitic capacitors completely.

Since M_1, M_2, M_5 and M_6 are turned on at the zero crossing point of resonant tank current, they are operated at the boundary condition of ZVS. Meanwhile, the resonant tank current should be calculated at switching instances to evaluate the soft switching performances for the remaining four switches. From Fig. 4, the turn-on moment of M_3 is $\omega_s t = \frac{\pi+\theta_1}{2}$ and the turn-on moment of M_8 is $\omega_s t = \varphi + \frac{\pi-\theta_1}{2}$.

$$i_{LC,pu}(\frac{\pi+\theta_1}{2}) = \frac{4\left[\sin^2\frac{\theta_1}{2} + M\sin\frac{\theta_2}{2}\sin(\varphi - \theta_1 + \frac{\theta_2}{2})\right]}{\pi X_{s,pu}} \quad (18)$$

$$i_{LC,pu}(\varphi + \frac{\pi - \theta_1}{2}) = \frac{4\left[\sin\frac{\theta_1}{2}\sin(\varphi - \frac{\theta_1}{2}) + M\sin^2\frac{\theta_2}{2}\right]}{\pi X_{s,pu}} \quad (19)$$

The following conclusions can be verified by math derivation: (18) and (19) are large than zero as long as equation (13) is true. Therefore, ZVS performance can be accomplished theoretically for the primary side leading legs switches (M_3 and M_4) and the secondary side lagging legs switches (M_7 and M_8).

Consequently, it can be concluded that soft switching can be achieved for all the eight switches when the DBSRC converter works in the boundary TPS mode. Additionally, there are no negative part of instantaneous input power p_i and output power p_o. Thus, the circulation energy and switching loss can be minimized.

D. PROPOSED UNIFIED BOUNDARY CONTROL WITH PHASE SHIFT COMPENSATION

As can be seen from the above analysis, the unified boundary control can be used to minimize circulating energy and switching loss. However, half of the switches are easy to lose ZVS since they are operated under the boundary conditions. In order to obtain the ZVS performance of all side switches and minimize conduction loss during dead time intervals, phase shift compensation scheme for both side is proposed.

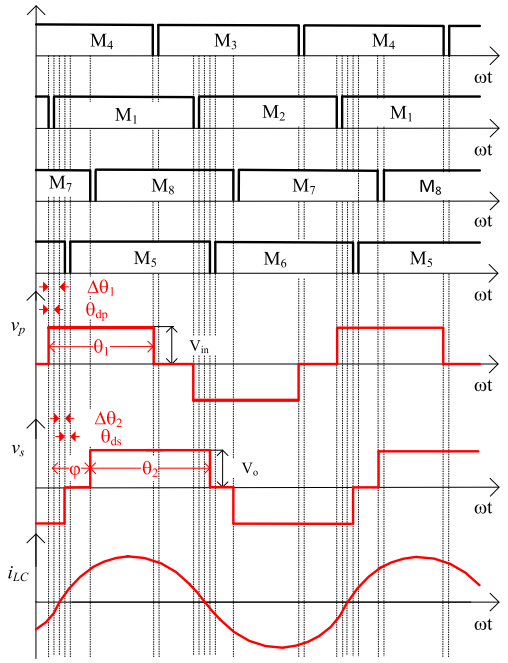

FIGURE 7. Typical operating waveforms of the DBSRC under unified boundary control with phase shift compensation.

In practice, the ZVS performance of those switches (M_1, M_2, M_5, M_7) can be achieved by rearranging the gating scheme with suitable dead time settings. Fig. 7 illustrates the switching actions of the DBSRC under unified boundary control including the effect of dead time and extra phase-shift compensations. As depicted in Fig. 7, the rising edge of v_p (turn-off moments of M_2) leads the zero crossing point of resonant tank current i_{LC} with a phase shift of $\Delta\theta_1$; the falling edge of v_s (turn-off moments of M_6) lags the zero crossing point of resonant tank current i_{LC} with a phase shift of $\Delta\theta_2$ respectively. Thus, an extra leading compensated phase-shift angle $\Delta\theta_1$ is added at primary side inner-bridge phase-shift; an extra lagging compensated phase-shift angle $\Delta\theta_2$ is added at secondary side inner-bridge phase-shift respectively. Hence, the first boundary condition can be obtained as

$$\varphi + \theta_2 = \pi + \Delta\theta_1 + \Delta\theta_2 \quad (20)$$

With the compensated phase shift, the two phase-shift angles θ_1 and θ_2 should also be modified accordingly to keep the balance in power transfer. As shown in Fig. 7, the fundamental component of v_p' leads the zero crossing point of resonant tank current i_{LC} with a phase-shift angle of $\frac{\pi-\theta_1}{2} + \Delta\theta_1$. Based on (5), the secondary zero circulating energy boundary condition can be given as

$$i_{LC,pu}(\frac{\pi - \theta_1}{2} + \Delta\theta_1) = 0 \quad (21)$$

By substituting (20) into (21), an simplified expression can be obtained as

$$\theta_1 = \Delta\theta_1 + \arccos\left[\cos\Delta\theta_1 + M(\cos(\theta_2 - \Delta\theta_2) - \cos\Delta\theta_2)\right] \quad (22)$$

Based on the above analysis, under the unified boundary TPS control with phase shift compensation scheme, the output power can be still controlled solely by the external phase-shift φ. The other two phase-shift angles (θ_1 and θ_2) can be obtained by φ from (20) and (22).

After phase shift compensations, the sufficient ZVS conditions for switches M_1 and M_5 are formulated as (23) and (24), respectively [29].

$$\begin{cases} \Delta\theta_1 \geq \theta_{dp} \\ \int_{-\frac{\Delta\theta_1}{\omega_s}}^{\frac{\theta_{dp}-\Delta\theta_1}{\omega_s}} -\sqrt{2}nI_{LCr}\sin(\omega_s t)dt \geq Q_p \end{cases} \quad (23)$$

$$\begin{cases} \Delta\theta_2 \geq 0 \\ \int_{\frac{\Delta\theta_2}{\omega_s}}^{\frac{\theta_{ds}+\Delta\theta_2}{\omega_s}} \sqrt{2}I_{LCr}\sin(\omega_s t)dt \geq Q_s \end{cases} \quad (24)$$

where Q_p and Q_s are the accumulated switching charges on the primary side and the secondary side, respectively. They are determined by the total parasitic capacitors and the change of drain-source voltage. θ_{dp} and θ_{ds} are the dead-time angles of gate drivers for each side, respectively. Based on (23) and (24), suitable compensated phase shifts can be selected to achieve ZVS for M_1 and M_5 over a wide output power range. Meanwhile, a small dead time can be set to prevent the occurrence of the shoot-through issue.

TABLE 1. Comparison of proposed control scheme with previous papers.

	Proposed control	DBSRC in [13]	DBSRC in [27]	DBSRC in [28]	DBSRC in [29]
Symmetric in driving signal	Yes	Yes	Yes	No	Yes
Number of control variables	3	1	3	3	4
Switching frequency	fixed	fixed	fixed	fixed	variable
Mode transition in control	No	No	Yes	Yes	Yes
Control Complexity	low	low	medium	medium	high
Softer-switching	Yes	not at light load	not at light load	not at light load	Yes
Circulating energy	No	Yes	Yes	Yes	No
Total efficiency	high	low at light load	medium	medium	high

E. COMPARISON

The general comparison of the proposed control with the previous papers are summarized in Table 1. In general, the proposed control strategy extends the soft-switching range and reduces the circulation energy effectively for the whole load range at low control complexity. Although scheme given in [29] is also effective for soft-switching improvement and zero circulating energy modulation, it increases the difficulty and cost of control parameter optimization with four control variables.

IV. DESIGN EXAMPLE BASED ON STEADY STATE ANALYSIS

A. DESIGN POINT

According to the steady-state analysis equations presented in Section II and III, relationship curves are obtained and used in designing a DBSRC converter. Based the design curves, the approximately optimal parameters needed to be chosen include M (converter gain), F (normalized switching frequency) and Q (rated load quality factor). The specifications of the converter to be designed are listed in Table 2.

TABLE 2. Specification of designed converter.

Parameter	Value
Maximum input voltage $V_{in,max}$	400V
Minimum input voltage $V_{in,min}$	360V
Nominal input voltage $V_{in,n}$	380V
Nominal output voltage V_o	120V
Rated output power P_R	500W
Switching frequency f_s	80kHz

In order to obtain high efficiency and optimum performance, the voltage gain at nominal input voltage is selected at unity gain, i.e., $M_n = 1$. With the nominal input voltage $V_{in,n} = 380$ V and $V_o = 120$ V, the primary side reflected input voltage is $V'_{in,n} = V_{in,n}M_n$. Therefore, the turns ratio of the high frequency transformer is found as $n = \frac{V_o}{V'_{in,n}} = \frac{12}{38}$. The maximum converter gain is: $M_{\max} = \frac{V_o}{nV_{in,\min}} = 1.056$. The minimum converter gain is: $M_{\min} = \frac{V_o}{nV_{in,\max}} = 0.95$.

Since the two switches at the same bridge leg are operated alternatively at almost 50% duty cycle with necessary dead-time. The voltage and current ratings of the primary side switches and secondary side switches can be calculated as (25) and (26), respectively.

$$\begin{cases} V_{DSp} = V_{in,\max} \\ I_{Dp} = \dfrac{nI_{LCr,\max}}{\sqrt{2}} \end{cases} \tag{25}$$

$$\begin{cases} V_{DSs} = V_o \\ I_{Ds} = \dfrac{I_{LCr,\max}}{\sqrt{2}} \end{cases} \tag{26}$$

With other converter parameters fixed, rated load quality factor Q should be selected to minimize both rms tank currents and the size of resonant tank capacitor and inductor. Fig. 8(a) presents the relationship between resonant tank rms current and voltage gain for different Q with normalized switching frequency $F = 1.26$. Fig. 8(b) shows the relationship between resonant tank capacitor peak voltage and voltage gain for different Q with $F = 1.26$. It is seen that using a small value of Q is able to reduce the resonant tank rms current and resonant tank capacitor peak voltage, even not significantly. Meanwhile, Q is proportional to the value of L_k and inversely proportional to the value of C_k [13], [14]. Thus, Q is expected to be small to reduce size of magnetic components and have better circuit performance. After some iterations, a compromised $Q = 1$ at design point is selected.

Usually the normalized switching frequency F is chosen to be larger than one but close to one to achieve an inductive resonant current for ZVS operation in two bridges and will not bring up large circulation current at same time. Fig. 8(c) illustrates the relationship between resonant tank rms current and voltage gain for different F with $Q = 1$. Fig. 8(d) presents the relationship between resonant tank capacitor peak voltage and voltage gain for different F with $Q = 1$. Fig. 8(e) plots the relationship between normalized output power with soft switching operation and voltage gain for different F with $Q = 1$. It is seen that using a small value of F is able to reduce the resonant tank rms current and resonant tank capacitor peak voltage, but will reduce the power regulation range. The value of F might be adjusted iteratively for optimum converter performance as long as the soft-switching operation is secured. Based on the aforementioned discussions, a trade-off value with $F = 1.26$ at design point is selected. And the resonant tank can be found as:

$$L_k = \frac{QFV_o^2}{\omega_s P_o} = 72.3\mu\text{H} \tag{27}$$

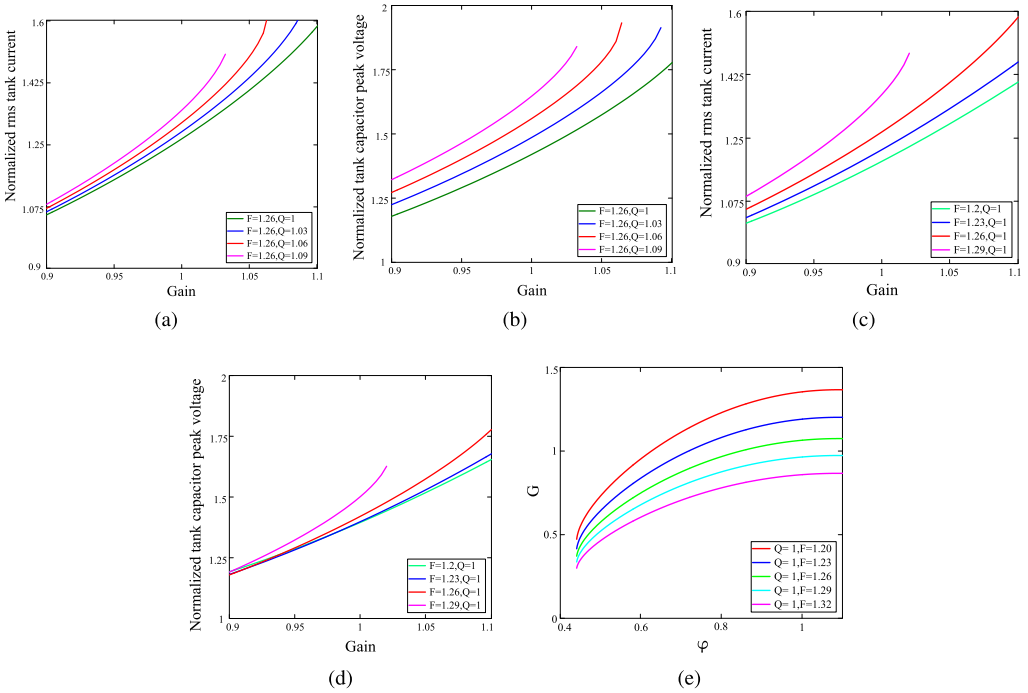

FIGURE 8. (a) Normalized rms tank current versus converter gain M with $F = 1.26$ for different values of Q. (b) Normalized tank capacitor peak voltage versus converter gain M with $F = 1.26$ for different values of Q. (c) Normalized rms tank current versus converter gain M with $Q = 1$ for different values of F. (d) Normalized tank capacitor peak voltage versus converter gain M and $Q = 1$ for different values of F. (e) Power level index versus external phase-shift φ with $Q = 1$ and $M = 1.056$ for different values of F.

$$C_k = \frac{FP_o}{\omega_s Q V_o^2} = 87n\text{F} \tag{28}$$

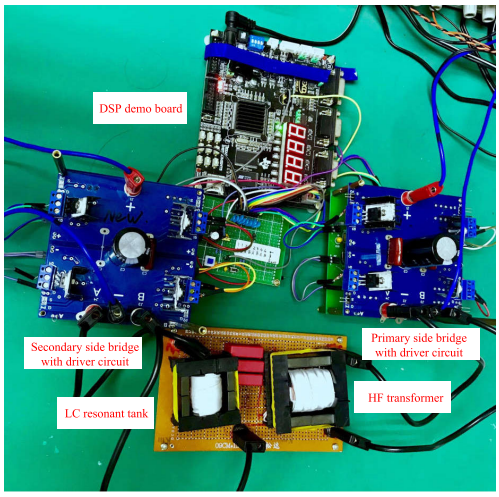

FIGURE 9. The layout of the experimental test.

TABLE 3. Main components parameters.

Device	Parameter/Value
Controller	DSP TMS320F28335 by TI
Primary side MOSFETs	IPP60R099P7(600 V, 31 A, 99 mΩ)
Secondary side MOSFETs	IPP320N20N(200 V, 31 A, 32 mΩ)
Gate driver	IR21814 by IR
Inductor L_k	72.3 μH(ETD39)
Transformer turn ratio	12:38 (ETD49)
Capacitor C_k	87 nF (MKP)

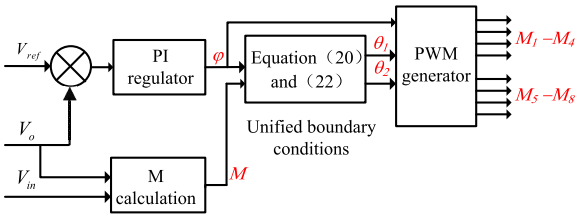

FIGURE 10. Control block diagram of the proposed control scheme.

B. EXPERIMENTAL RESULTS

A 500W prototype converter with the proposed control strategy was built and tested in the lab. A photograph of the experiment setup is shown in Fig. 9. The specifications of the main components to implement the circuit are listed in Table 3. All the control scheme is realized by DSP controller TMS320F28335. The detailed control diagram of the proposed boundary control is shown in Fig. 10. The output voltage is stabilized by a simple PI compensator. The phase-shift φ can be adjusted dynamically with the output of the PI regulator to keep the balance in input/output power. Meanwhile, the voltage gain M is calculated online with the input/output voltage sampled singles. Then, the obtained

phase-shift φ and voltage gain M are fed into the boundary conditions to calculate the other two variables θ_1 and θ_2. Finally, the driving singles are generated by the PWM generator in DSP controller according to the obtained three control variables. The implementation of closed-loop control is not hard, and there is no need of complex calculations and working mode transition.

The resonant tank current is large enough to accomplish ZVS during the dead-time intervals at lower voltage side. Hence there is no need to compensate phase shift at the lower voltage side (i.e. $\Delta\theta_2 = 0$ rad). In order to suppress circulating energy, an minimize compensated phase shift is designed for all switchers operating in ZVS under 30% to full load power range. The compensated phase-shift at the higher voltage side and the dead time can be calculated as $\Delta\theta_1 = 0.1$ rad and $\theta_{dp} = \theta_{ds} = 150$ ns according to (23) and (24).

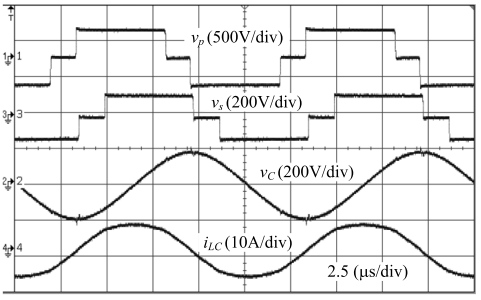

(a)

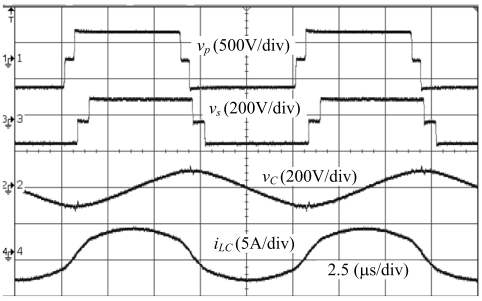

(b)

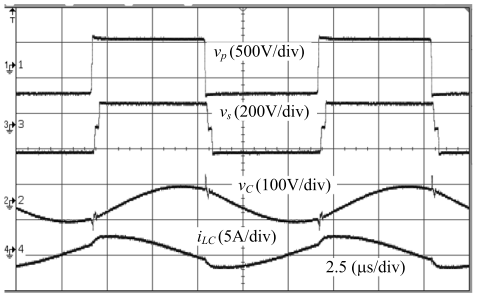

(c)

FIGURE 11. Experimental steady-state plots at $V_{in} = 380$V (from top to bottom: primary HF ac voltage v_p, secondary HF ac voltage v_s, resonant tank capacitor voltage v_c and resonant tank current i_{LC}). (a) $P_o = 500$ W. (b) $P_o = 300$ W. (c) $P_o = 150$ W.

The steady-state plots obtained from experiments are depicted in Fig. 11, in which the full, 60% and 30% load conditions of nominal primary side voltage are investigated for charging mode. In addition to adding a small phase shift at primary high-voltage side, the positive rising edge of primary side ac voltage and negative falling edge of secondary ac voltage almost align with zero crossing point of resonant tank current. Thus, the circulating energy is small. There is no parasitic-induced ringing at the rising edges of both side ac voltage, which indicates ZVS. The resonant tank current and capacitor voltage are both sinusoidal waveforms at full load. The resonant tank current is an approximate sinusoidal waveforms with a little distortion at light load. The inner-bridge phase-shift and the external phase-shift will increase at the same time as the output power increases, that agrees with phasor analysis.

Fig. 12 illustrates the steady-state experiment waveforms at different primary side voltage under full load. With non-unity voltage gain, the circulating energy is also small and ZVS performance are achieved for all eight switchers. As shown in Fig. 12, the positive pulse width of primary side voltage is longer than that of secondary ac voltage for $M > 1$ (i.e. $V_{in} = 360$ V); the positive pulse width of primary side voltage is shorter than that of secondary ac voltage for $M < 1$ (i.e. $V_{in} = 400$ V). The output power is mainly controlled by the external phase-shift. The experiment results also agree with phasor analysis.

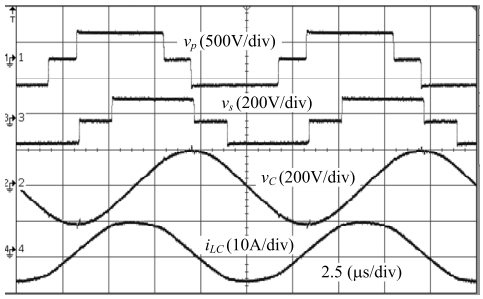

(a)

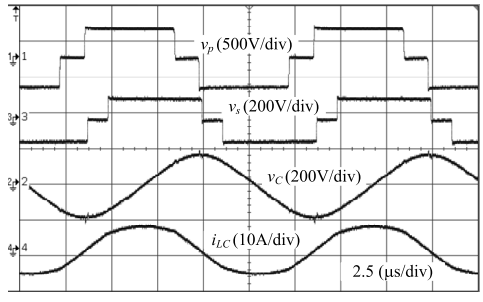

(b)

FIGURE 12. Experimental steady-state plots at different input voltage under full load (from top to bottom: primary HF ac voltage v_p, secondary HF ac voltage v_s, resonant tank capacitor voltage v_c and resonant tank current i_{LC}). (a) $V_{in} = 360$ V. (b) $V_{in} = 400$ V.

The waveforms of switching behaviour obtained from experiments are shown in Fig. 13 and Fig. 14, in which the full load and 30% load conditions of 380V input voltage

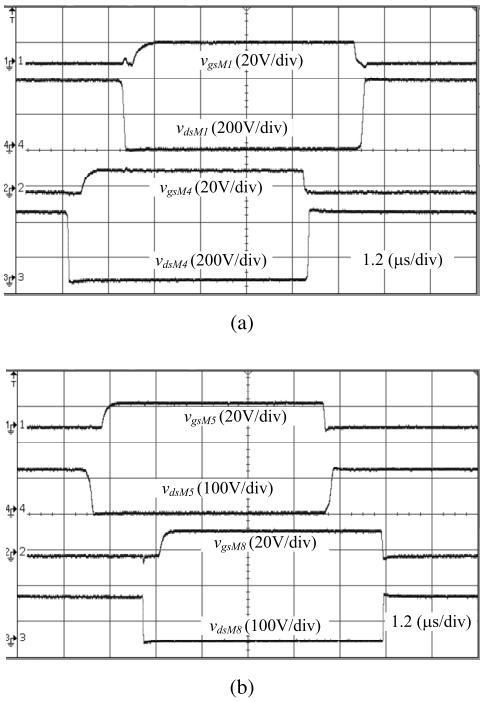

FIGURE 13. Experimental switching waveforms at $V_{in} = 380$ V, $V_o = 120$ V, $P_o = 500$ W. (a) Primary side switches M_1 and M_4 (from top to bottom: driver signal v_{gsM1}, drain to source voltage v_{dsM1}), driver signal v_{gsM4}, drain to source voltage v_{dsM4}). (b) Secondary side switches M_5 and M_8 (from top to bottom: driver signal v_{gsM5}, drain to source voltage v_{dsM5}), driver signal v_{gsM8}, drain to source voltage v_{dsM8}).

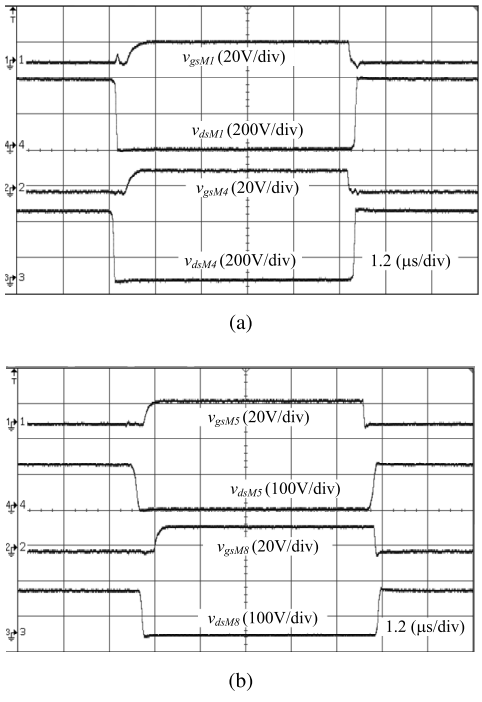

FIGURE 14. Experimental switching waveforms at $V_{in} = 380$ V, $V_o = 120$ V, $P_o = 150$ W. (a) Primary side switches M_1 and M_4 (from top to bottom: driver signal v_{gsM1}, drain to source voltage v_{dsM1}), driver signal v_{gsM4}, drain to source voltage v_{dsM4}). (b) Secondary side switches M_5 and M_8 (from top to bottom: driver signal v_{gsM5}, drain to source voltage v_{dsM5}), driver signal v_{gsM8}, drain to source voltage v_{dsM8}).

are tested respectively. It can be seen that ZVS performance is accomplished for all the switchers as the drain to source voltage have fallen down to zero before the gate driver are applied.

The measured converter efficiency curves with SPS, MCT and proposed control under different voltage gain and output power are listed in Fig. 15. The selection of control variable is not unified with MCT, which is according to the range of voltage gain. In case of M=1 in Fig. 15(b), MCT has same control condition as the conventional SPS control and hence the two efficiency curves are overlapping. With the proposed control scheme, at the full load condition, the measured efficiency are 95.6%, 95.9% and 95.8% for $V_{in} = 360$ V, $V_{in} = 380$ V, and $V_{in} = 400$ V respectively. The peak efficiency of the proposed control at 96.1% is achieved under $P_o = 400$ W and $V_{in} = 380$ V. By employing the proposed control scheme, the efficiency of the prototype is higher than those with other two control schemes and can be maintained over 88% for whole converter gain and load range. It can be seen that relatively high efficiency is maintained under MCT and proposed control over a wide range of load conditions, while the SPS control have poor performance when the voltage gain was away from the design point. Generally, the improvement of efficiency with proposed control over that with SPS control is relatively small for high load, especially at unity converter gain. When the converter gain is away from unity, the merits

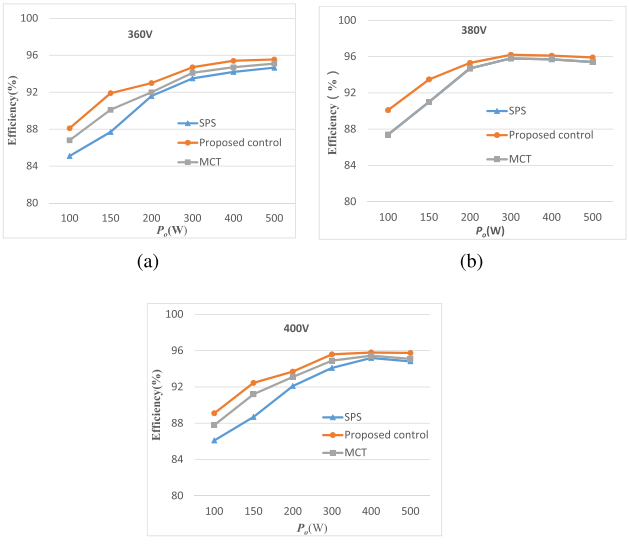

FIGURE 15. Measured converter efficiency curves with SPS, MCT and proposed control at different output powers. (a) $V_{in} = 360$ V, $V_o = 120$ V. (b) $V_{in} = 380$ V, $V_o = 120$ V. (c) $V_{in} = 400$ V, $V_o = 120$ V.

of the proposed control in terms of reduced rms resonant current and ZVS becomes apparent, especially at medium and light load level. For an example, the efficiency of proposed control has an improvement of more than 3% at $P_o = 100$ W for $M = 0.95$ and $M = 1.056$. With the benefit of minimized

current operation, the converter efficiency of MCT control is slightly lower than the one with proposed control at whole load range.

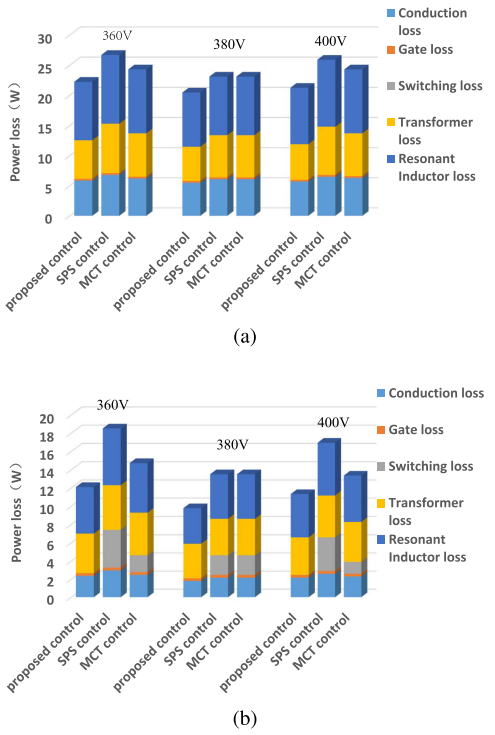

FIGURE 16. Loss distribution with SPS, MCT and proposed control at different input voltages and output powers. (a) $P_o = 500$ W. (b) $P_o = 150$ W.

In Fig. 16, comparison between the proposed control, MCT and SPS control are made in terms of the loss breakdown under different input voltage and load level. The main sources of loss considered include inductor loss, transformer loss, conduction loss of switches, gate loss and switching loss. Both copper loss and iron loss of resonant inductor and HF transformer are calculated by using the datasheets from manufacturers. Due to almost zero switching loss and low circulation energy, the converter is able to maintain lower power loss even with the variations of input voltage and load. It is seen in Fig. 16(a) that with proposed control the copper loss and conduction loss is slightly reduced at full load level. Due to high circulating power and hard switching characteristic, the switching loss of SPS control increases significantly at light load while the total loss of proposed control can be maintained at a lower level as shown in Fig. 16(b). The difference of total power loss between the proposed control and SPS control become larger when the voltage gain is away from unity as shown in Fig. 16. Meanwhile, compared with the MCT control, the efficiency optimization of the proposed control is not significant. The potential reasons might be: (1) only two switches will suffer from hard switching under light load condition with MCT; (2) the MCT also has less copper loss and conduction loss.

The comparison of theoretical calculation, simulation and experimental measurements of the key steady-state working

TABLE 4. Comparison of steady-state operation at $V_{in} = 380$V, $V_o = 120$V.

Power		φ (°)	i_{LCp} (A)	i_{LCr} (A)	V_{Cp} (V)
500 W	Theory	49.1	7.06	5.23	172.23
	Simulation	49.3	7.12	5.25	175.89
	Experiment	50.5	7.15	5.26	180.5
300 W	Theory	25.09	3.91	2.95	100.1
	Simulation	26.2	4.01	3.07	103.9
	Experiment	27.4	4.10	3.17	110
150 W	Theory	14.6	1.42	1.14	38.1
	Simulation	14.8	1.51	1.20	40.7
	Experiment	17.7	1.97	1.42	52.5

TABLE 5. Comparison of steady-state operation at $V_{in} = 360$V, $V_o = 120$V.

Power		φ (°)	i_{LCp} (A)	i_{LCr} (A)	V_{Cp} (V)
500 W	Theory	60.01	7.81	5.80	182.23
	Simulation	60.20	7.87	5.83	187.89
	Experiment	61.05	7.92	5.91	190.5
300 W	Theory	35.62	3.92	2.95	101.1
	Simulation	35.9	3.93	3.04	102.9
	Experiment	36.64	4.13	3.13	107
150 W	Theory	24.64	1.87	1.48	39.7
	Simulation	24.89	1.89	1.50	41.72
	Experiment	26.98	2.37	1.783	58.5

parameters are listed in Table 4 and Table 5. In the region of high load, the simulation and experimental results have good match with the theoretical calculation values, which can validate the effectiveness of FHA based analysis. Compared with the theoretical calculation and simulation results, the experimental value shows a certain degree of deviation under light load level, which can be due to the non-ideal parasitic parameters of actual circuit components and the high order harmonics of the two side high frequency ac voltage.

V. CONCLUSION

In this paper, a unified boundary control is proposed based on TPS gating scheme to DBSRC, which aims to minimize the circulating current and improve the overall converter efficiency. Meanwhile, a duty cycle compensation feature is also proposed to keep ZVS operation and reduce conduction loss. The proposed control strategy is unified for the whole variation range of load, input/output voltage and with simple calculation. Validation has been done successfully through tests on a physical converter. It can be concluded that with minimum circulating energy control as the objective, the control scheme have better performance at a wide range of operation condition than conventional SPS and MCT controls. Loss analysis indicates the improvement is attributed to low rms current and negligible switching loss. In the future work, more efforts would be put on the integration of the proposed control with voltage-current feedback and their implementation.

APPENDIX

The normalized fundamental voltage phasors of v'_p and v_s can be expressed as (29) and (30), respectively.

$$\mathbf{V'_{P,1pu}} = \frac{4}{\pi}\sin(\frac{\theta_1}{2})e^{j(\omega_s t-\frac{\pi}{2})} \tag{29}$$

$$\mathbf{V_{S,1pu}} = \frac{4M}{\pi}\sin(\frac{\theta_2}{2})e^{j\left[\omega_s t-(\varphi+\frac{\theta_2-\theta_1}{2})-\frac{\pi}{2}\right]} \tag{30}$$

By using superposition theorem, the normalized resonant tank current phasor can be evaluated as

$$\begin{aligned}\mathbf{I_{LC,pu}} &= \frac{\mathbf{V'_{P,1pu}} - \mathbf{V_{S,1pu}}}{jX_{s,pu}} \\ &= \frac{4\left[M\sin(\frac{\theta_2}{2})e^{j(\omega_s t-(\varphi+\frac{\theta_2-\theta_1}{2}))} - \sin(\frac{\theta_1}{2})e^{j(\omega_s t)}\right]}{\pi X_{s,pu}}\end{aligned} \tag{31}$$

Then, the normalized resonant tank current $i_{LC,pu}$ in time domain can be obtained as (32).

$$i_{LC,pu}(\omega_s t) = \Re\left\{\mathbf{I_{LC,pu}}\right\} \tag{32}$$

By using (5), the normalized root-mean-square (rms) current $I_{LCr,pu}$ can be derived as

$$I_{LCr,pu} = \sqrt{\frac{1}{\pi}\int_0^{\pi}\left[i_{LC,pu}(\omega_s t)\right]^2 d\omega_s t} \tag{33}$$

The normalized resonant tank capacitor peak voltage can be derived as follows:

$$V_{Cp,pu} = \frac{\sqrt{2}I_{LCr,pu}}{\omega_s C_k Z_B} = \frac{\sqrt{2}I_{LCr,pu}Q}{F} \tag{34}$$

REFERENCES

[1] W. Chen, F. C. Lee, M. M. Jovanovic, and J. A. Sabate, "A comparative study of a class of full bridge zero-voltage-switched PWM converters," in *Proc. APEC*, 1995, pp. 893–899.
[2] G. Hua, C.-S. Leu, Y. Jiang, and F. C. Y. Lee, "Novel zero-voltage-transition PWM converters," *IEEE Trans. Power Electron.*, vol. 9, no. 2, pp. 213–219, Mar. 1994.
[3] R. W. A. A. De Doncker, D. M. Divan, and M. H. Kheraluwala, "A three-phase soft-switched high-power-density DC/DC converter for high-power applications," *IEEE Trans. Ind. Appl.*, vol. 27, no. 1, pp. 63–73, Jan. 1991.
[4] M. Jain, M. Daniele, and P. K. Jain, "A bidirectional DC-DC converter topology for low power application," *IEEE Trans. Power Electron.*, vol. 15, no. 4, pp. 595–606, Jul. 2000.
[5] K. Wang, C.-Y. Lin, L. Zhu, D. Qu, F. C. Lee, and J.-S. Lai, "Bi-directional DC to DC converters for fuel cell systems," in *Proc. IEEE Power Electron. Transp.*, Jan. 1998, pp. 47–51.
[6] S. Inoue and H. Akagi, "A bidirectional isolated DC–DC converter as a core circuit of the next-generation medium-voltage power conversion system," *IEEE Trans. Power Electron.*, vol. 22, no. 2, pp. 535–542, Mar. 2007.
[7] Y. Wang, K. Wang, C. Li, Z. Zheng, and Y. Li, "System-level efficiency evaluation of isolated DC/DC converters in power electronics transformers for medium-voltage DC systems," *IEEE Access*, vol. 7, pp. 48445–48458, 2019.
[8] H. K. Krishnamurthy and R. Ayyanar, "Building block converter module for universal (AC-DC, DC-AC, DC-DC) fully modular power conversion architecture," in *Proc. IEEE PESC*, Jun. 2007, pp. 483–489.
[9] H. Qin and J. W. Kimball, "Solid-state transformer architecture using AC–AC dual-active-bridge converter," *IEEE Trans. Ind. Electron.*, vol. 60, no. 9, pp. 3720–3730, Sep. 2013.
[10] S. Falcones, X. Mao, and R. Ayyanar, "Topology comparison for solid state transformer implementation," in *Proc. IEEE PES Gen. Meeting*, Jul. 2010, pp. 1–8.
[11] I. D. Jitaru, "A 3 kW soft switching DC-DC converter," in *Proc. IEEE APEC*, Feb. 2000, pp. 86–92.
[12] A. K. Jain and R. Ayyanar, "Pwm control of dual active bridge: Comprehensive analysis and experimental verification," *IEEE Trans. Power Electron.*, vol. 26, no. 4, pp. 1215–1227, Apr. 2011.
[13] X. Li and A. K. S. Bhat, "Analysis and design of high-frequency isolated dual-bridge series resonant DC/DC converter," *IEEE Trans. Power Electron.*, vol. 25, no. 4, pp. 850–862, Apr. 2010.
[14] X. Li, "A LLC-type dual-bridge resonant converter: Analysis, design, simulation, and experimental results," *IEEE Trans. Power Electron.*, vol. 29, no. 8, pp. 4313–4321, Aug. 2014.
[15] S. Bhowmick and A. K. Bhat, "A fixed-frequency LCC-type resonant converter with inductive output filter using a modified gating scheme," in *Proc. IEEE ICAECT*, Jan. 2014, pp. 140–145.
[16] N. Harischandrappa and A. K. Bhat, "A fixed-frequency *LCL*-type series resonant converter with a capacitive output filter using a modified gating scheme," *IEEE Trans. Ind. Appl.*, vol. 50, no. 6, pp. 4056–4064, Jan. 2014.
[17] H. Chen and A. K. S. Bhat, "Analysis and design of a dual-bridge series resonant DC-to-DC converter for capacitor semi-active battery-ultracapacitor hybrid storage system," in *Proc. IEEE ISIE*, Jun. 2014, pp. 1788–1793.
[18] S. Shao, H. Chen, X. Wu, J. Zhang, and K. Sheng, "Circulating current and ZVS-on of a dual active bridge DC-DC converter: A review," *IEEE Access*, vol. 7, pp. 50561–50572, 2019.
[19] B. Zhao, Q. Song, W. Liu, and Y. Sun, "Overview of dual-active-bridge isolated bidirectional DC–DC converter for high-frequency-link power-conversion system," *IEEE Trans. Power Electron.*, vol. 29, no. 8, pp. 4091–4106, Aug. 2014.
[20] B. Zhao, Q. Song, W. Liu, G. Liu, and Y. Zhao, "Universal high-frequency-link characterization and practical fundamental-optimal strategy for dual-active-bridge DC-DC converter under PWM plus phase-shift control," *IEEE Trans. Power Electron.*, vol. 30, no. 12, pp. 6488–6494, Dec. 2015.
[21] F. Krismer and J. W. Kolar, "Closed form solution for minimum conduction loss modulation of DAB converters," *IEEE Trans. Power Electron.*, vol. 27, no. 1, pp. 174–188, Jan. 2012.
[22] G. G. Oggier, G. O. Garcia, and A. R. Oliva, "Modulation strategy to operate the dual active bridge DC-DC converter under soft switching in the whole operating range," *IEEE Trans. Power Electron.*, vol. 26, no. 4, pp. 1228–1236, Apr. 2011.
[23] D. Sha, J. Zhang, and Y. Xu, "Improved boundary operation for voltage-fed semi-DAB with ZVS achievement and nonactive power reduction," *IEEE Trans. Ind. Electron.*, vol. 64, no. 8, pp. 6179–6189, Aug. 2017.
[24] W. Choi, K.-M. Rho, and B.-H. Cho, "Fundamental duty modulation of dual-active-bridge converter for wide-range operation," *IEEE Trans. Power Electron.*, vol. 31, no. 6, pp. 4048–4064, Jun. 2016.
[25] G. Xu, D. Sha, J. Zhang, and X. Liao, "Unified boundary trapezoidal modulation control utilizing fixed duty cycle compensation and magnetizing current design for dual active bridge DC–DC converter," *IEEE Trans. Power Electron.*, vol. 32, no. 3, pp. 2243–2252, Mar. 2017.
[26] H. Shi, H. Wen, Y. Hu, and L. Jiang, "Reactive power minimization in bidirectional DC–DC converters using a unified-phasor-based particle swarm optimization," *IEEE Trans. Power Electron.*, vol. 33, no. 12, pp. 10990–11006, Dec. 2018.
[27] L. Corradini, D. Seltzer, D. Bloomquist, R. Zane, D. Maksimović, and B. Jacobson, "Minimum current operation of bidirectional dual-bridge series resonant DC/DC converters," *IEEE Trans. Power Electron.*, vol. 27, no. 7, pp. 3266–3276, Jul. 2012.
[28] S. Hu, X. Li, and A. K. S. Bhat, "Operation of a bidirectional series-resonant converter with minimized tank current and wide ZVS range," *IEEE Trans. Power Electron.*, vol. 34, no. 1, pp. 904–915, Jan. 2019.
[29] M. Yaqoob, K. H. Loo, and Y. M. Lai, "A four-degrees-of-freedom modulation strategy for dual-active-bridge series-resonant converter designed for total loss minimization," *IEEE Trans. Power Electron.*, vol. 34, no. 2, pp. 1065–1081, Feb. 2019.

GUO CHEN received the B.Eng. degree in electrical information engineering from the Anhui University of Science and Technology, Huainan, China, in 2003, and the M.S. degree from the South China University of Technology, Guangzhou, China, in 2006. He is currently pursuing the Ph.D. degree in power electronics with the Macau University of Science and Technology, Macau.

From 2006 to 2009, he worked as a Power Supply Design Engineer with Emerson Network Power Limited, Shenzhen, China. He joined the Faculty of Electrical and Information Technology, Zhongshan Polytechnic, Zhongshan, China, in 2009, where he is currently an Associate Professor. His research interest includes high frequency isolated bidirectional DC-DC converters for renewable energy systems.

XIAODONG LI (Senior Member, IEEE) received the B.Eng. degree in electrical engineering from Shanghai Jiao Tong University, Shanghai, China, in 1994, and the M.A.Sc. and Ph.D. degrees in electrical engineering from the University of Victoria, Victoria, BC, Canada, in 2004 and 2009, respectively.

From 1994 to 2002, he worked with Hongwan Diesel Power Corporation, Zhuhai, China, as an Electrical Engineer, where he conducted maintenance of the diesel power generation system. He joined the Faculty of Information Technology, Macau University of Science and Technology, Macau, in 2009, where he is currently an Associate Professor. He has authored or coauthored more than 50 articles in international conference proceedings and journals and holds three U.S. patens and five Australia Innovation patents. His research interests include high frequency power converters and its applications.

Dr. Li received the IEEE PES Best Paper Prize, in 2007, and the BOC Excellent Research Award from the Macau University of Science and Technology, in 2013.

SHENGZHI ZHOU received the B.Sc. and M.Sc. degrees from the Macau University of Science and Technology, Macau, in 2016 and 2018, respectively, where he is currently pursuing the Ph.D. degree in power electronics. His research interests include high frequency isolated resonant converters and its control.